AGU ADVANCING EARTH AND SPACE SCIENCE

Geophysical Research Letters

RESEARCH LETTER
10.1029/2021GL093372

Key Points:

- The P-wave velocity structure of a shale watershed under compression is imaged
- Seismic images show little evidence of the expected bowtie structure
- Results are explained by greater importance of chemical weathering than fracturing in determining seismic velocities in shale landscapes

Supporting Information:

Supporting Information may be found in the online version of this article.

Correspondence to:

A. Nyblade,
aan2@psu.edu

Citation:

Ma, L., Oakley, D., Nyblade, A., Moon, S., Accardo, N., Wang, W., et al. (2021). Seismic imaging of a shale landscape under compression shows limited influence of topography-induced fracturing. *Geophysical Research Letters*, *48*, e2021GL093372. https://doi.org/10.1029/2021GL093372

Received 12 MAR 2021
Accepted 30 JUL 2021

Seismic Imaging of a Shale Landscape Under Compression Shows Limited Influence of Topography-Induced Fracturing

Lisa Ma[1], David Oakley[2], Andrew Nyblade[1], Seulgi Moon[3], Natalie Accardo[1], Wei Wang[2], Xin Gu[2], Kristen Brubaker[4], Gregory J. Mount[5], Brandon Forsythe[2], Bradley J. Carr[6], and Susan L. Brantley[1,2]

[1]Department of Geosciences, Pennsylvania State University, University Park, PA, USA, [2]Earth and Environmental Systems Institute, Pennsylvania State University, University Park, PA, USA, [3]Department of Earth, Planetary and Space Sciences, University of California, Los Angeles, Los Angeles, CA, USA, [4]Department of Environmental Studies, Hobart and William Smith Colleges, Geneva, NY, USA, [5]Broward County Environmental Protection and Community Resilience Division, Broward County, Fort Lauderdale, FL, USA, [6]Department of Geology and Geophysics, University of Wyoming, Laramie, WY, USA

Abstract We used seismic refraction to image the P-wave velocity structure of a shale watershed experiencing regional compression in the Valley and Ridge Province (USA). From estimates showing strong compressional stress, we expected the depth to unweathered bedrock to mirror the hill-valley-hill topography ("bowtie pattern") by analogy to seismic velocity patterns in crystalline bedrock in the North American Piedmont that also experience compression. Previous researchers used failure potentials calculated for strong compression in the Piedmont to suggest fractures are open deeper under hills than valleys to explain the "bowtie" pattern. Seismic images of the shale watershed, however, show little evidence of such a "bowtie." Instead, they are consistent with weak (not strong) compression. This contradiction could be explained by the greater importance of infiltration-driven weathering than fracturing in determining seismic velocities in shale compared to crystalline bedrock, or to local perturbations of the regional stress field due to lithology or structures.

Plain Language Summary Rock mechanic theory suggests that the depth to crystalline bedrock under hill-valley-hill landscapes mirrors the land surface when the landscape experiences strong compression. We tested for this in a region of compression for a watershed on shale and found the depth pattern was consistent only with weak compression. This observation may be because infiltration and chemical weathering are more important than mechanical fracturing in controlling density of near-surface shale. Alternatively, local effects related to the last glacial advance or the differences in rock types might explain the observation. The depth of weathering (depth to bedrock) is apparently not only controlled by fracturing but rather is heavily influenced by hydrogeochemical processes on shale.

1. Introduction

The structure of the subsurface is largely unknown except at boreholes or roadcuts or through geophysical imaging (e.g., Gu, Mavko, et al., 2020; Holbrook et al., 2013; Oakley et al., 2021; Parsekian et al., 2015; Reibe et al., 2017; St. Clair et al., 2015; West et al., 2019). Recently, geophysicists discovered that seismic images in crystalline bedrock under crustal compression show a "bowtie" structure. Such a structure shows a seismic velocity pattern that mirrors the topography, with shallow depths (relative to an elevation datum) to unweathered bedrock under the valleys and deep depths under the ridgelines (St. Clair et al., 2015). For example, St. Clair et al. (2015) reported a bowtie pattern for almost the entire range of imaged velocities (i.e., <1,000–>4,000 m/s) for two landscapes developed on crystalline rock (Figures S1a and S1b). This pattern is of interest because it matches theoretical calculations of the potential for fracturing.

St. Clair et al. (2015) attributed the bowtie structure at two locations in the Piedmont Province of eastern North America (Pond Branch, MD; Calhoun, SC) to fracturing driven by coupling between tectonic stress and topography. They argued that topographic perturbation to a strong horizontal tectonic compression created the potential for opening fractures to greater depths under ridges than valleys when compared to an

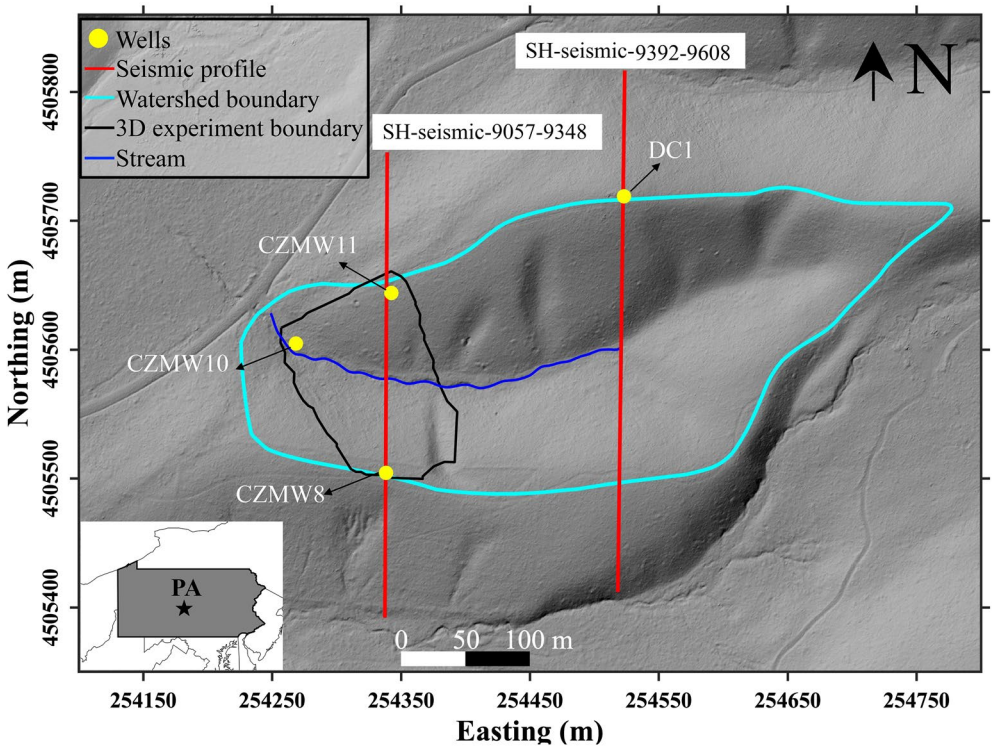

Figure 1. A grayscale hill shade map of the Shale Hills watershed showing seismic station and well locations. The 2D seismic refraction profiles used in this study are shown with red lines.

elevation datum (e.g., Moon et al., 2017; Slim et al., 2015). This "bowtie," observed for hill-valley-hill landscapes experiencing strong horizontal tectonic compression oriented orthogonal to the strike of the valley axis, was attributed to a decrease and an increase in the least compressive principal stress under ridges and valleys, respectively.

Here, we used travel-time refraction tomography to model the 2D P-wave velocity structure of a small shale watershed (Shale Hills) that was thought to be experiencing compression of similar magnitude to that of the two Piedmont watersheds (Figure 1). Furthermore, the relief-to-length ratio of Shale Hills is ~0.25, similar to values for the two Piedmont watersheds (Table S1). Shale Hills is located in the Valley and Ridge physiographic province ~170 km northwest of Pond Branch, one of the Piedmont watersheds (St. Clair et al., 2015). Based on five *in-situ* stress measurements compiled within ~500 km of Shale Hills, Slim et al. (2015) used a 2D stress model to show that the area is under a strong compressive horizontal tectonic stress of ~10 MPa at the surface, similar to Pond Branch. We thus predicted, by analogy to the observations at the two Piedmont watersheds, that Shale Hills would show strong evidence of a bowtie pattern.

We examined P-wave velocities (Vp) along two seismic refraction profiles crossing Shale Hills that are similar to the Piedmont transects. We compared the variations with predictions of shear failure potential from a 3D stress model based on values of ambient horizontal compression ranging from strong to weak. A comparison of the seismic images and fracture predictions allows evaluation of tectonic stress-induced fracturing as an explanation for depth of fracturing and weathering in shale.

2. Background

Shale Hills, a ~20 acre watershed developed primarily on Siluran Rose Hill shale in Pennsylvania (USA), hosts an ephemeral, westward-flowing stream (Brantley et al., 2018; Sullivan et al., 2016; West et al., 2013; Figure 1). The catchment is defined by a narrow valley and mostly sub-planar hillslopes. The average valley-to-ridge relief is ~30 m, ranging from 310 to 256 m above sea level (Herndon et al., 2018). The thickness of hand-augerable material, which we call mobile soil (but that includes some alluvium), ranges from 0.3 m

at ridge tops to 3 m in the valley (West et al., 2013). The mobile soil lies on top of a discontinuous layer of colluvium (West et al., 2013, 2019). The watershed receives about 1 m mean annual precipitation (MAP), of which half leaves as evapotranspiration. Of the rest, ~90% infiltrates and flows downslope at depths that are <10 meters below land surface (mbls). A small fraction infiltrates vertically to the regional groundwater table that lies at ~15–25 mbls under the ridges and emerges in the valley as the ephemeral stream (Sullivan et al., 2016).

3. Data

Data used in this study come from geophysical logs for a new borehole, CZMW11 (Figure 1, Supporting Information), and a seismic survey consisting of 4,200 seismic stations deployed in a ~140 × 160 m grid covering the western one-third of the watershed, along with linear profiles both connected to and separate from the grid (Figures 1 and S2; https://doi.org/10.7914/SN/YR_2018). Here, we focus on two linear profiles (SH-seismic-9392-9608; SH-seismic-9057-9348) extending across the ridges bounding the watershed and into adjacent watersheds (Figure 1). Details about the data collection and arrival time picking are in Supporting Information Ma (2020).

Profile SH-seismic-9392-9608, located on the eastern side of the watershed, is 440 m long and comprised of 216 seismic stations spaced 2 m apart that recorded 217 sledgehammer shots taken between seismic stations, and 23 shotgun shots spread at 20 m intervals along the profile (Figures 1 and S2). The profile intersects well DC1 on the northern ridge. Profile SH-seismic-9057-9348, located partially within the grid of stations, is 370 m long and is comprised of 180 stations that recorded 72 sledgehammer shots (Figures 1 and S2). The profile intersects wells CZMW8 on the southern ridge and CZMW11 on the northern ridge. Uncertainty in the hand-picked P-wave arrival times is 3–4 ms (Supporting Information).

4. Modeling

Seismic. P-wave arrival times were modeled using the ray-theory-based First Arrival Seismic Tomography (FAST) method (Zelt & Barton, 1998; Zelt et al., 2006). In this method, forward travel times are calculated using finite difference approximations to the eikonal equations (Vidale, 1990). A sparse least squares variant of the conjugate gradient method (Nolet, 1987) is employed in the inversion. Model regularization is achieved using smoothness constraints. After testing many combinations of model parameters, it was found that a 2 m cell size and a 0.5 m node spacing yielded smooth models that also minimized the data misfit for a reasonable range of smoothing parameters. Details of the modeling and selection of parameters are in Supporting Information and Ma (2020).

The starting model for the inversions was constructed using sonic logs from wells CZMW 8, 10, and 11, with velocities at each depth in the model selected to approximately match the average of the velocities in the boreholes (Figure S3). Starting models that included various velocity gradients over different depth intervals yielded similar inversion results (Ma, 2020). The highest velocity of 4,500 m/s, found at depths of 35–42 m in well CZMW11, was set as the maximum velocity allowed in the inversion.

Checkerboard tests were performed in which synthetic travel times were obtained by ray tracing through a model containing a checkerboard velocity pattern. Gaussian normally distributed noise was added to the synthetic travel times (with a mean of zero and a standard deviation of 2 ms to account for uncertainties up to 4 ms in arrival time picks). Inversions were then performed using the same parameters as the final models to determine if the checkerboard patterns could be resolved. In these tests, a range of checker parameters were used, including anomaly percentage, checker size, spacing, and depth (Ma, 2020).

Stress modeling. The three-dimensional topographic stress regime was calculated using the boundary element model Poly3D (Thomas, 1993) following procedures as in St. Clair et al. (2015) and Moon et al. (2017, 2020). The subsurface total stress fields were quantified as the sum of (a) ambient stress due to horizontal compression and gravity, and (b) stress perturbation from actual topography. We constrained the ambient stresses using a compilation of 33 *in-situ* stress measurements from the World Stress Map 2016 (Haimson, 1977; Heidbach et al., 2016; Figure S4; Table S2). The *in-situ* stress measurement sites were located ~ 120–500 km from Shale Hills. These distances are similar to the distances used by St. Clair et al. (2015)

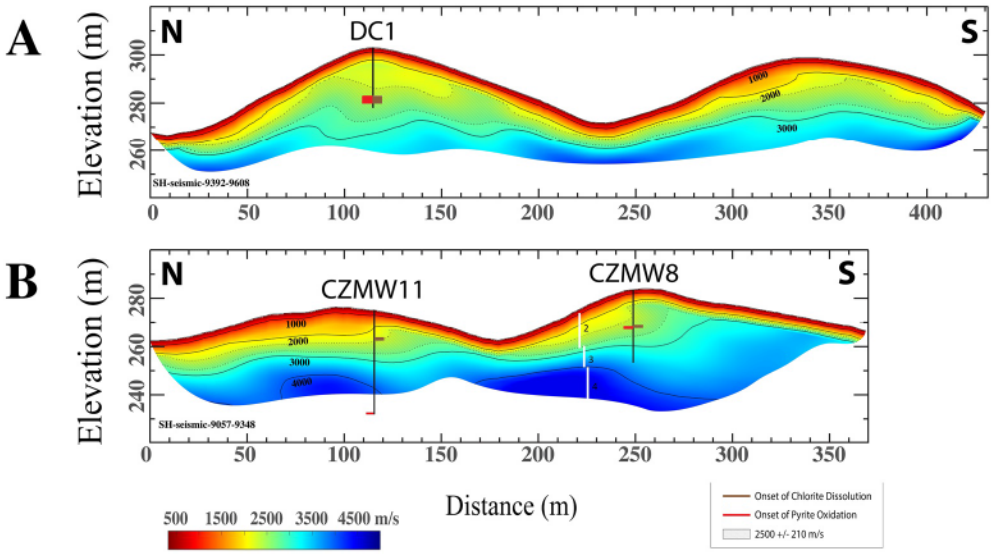

Figure 2. P-wave velocity models cropped to show only parts of the subsurface where velocities are resolved. (a) SH-seismic-9392-9608, (b) SH-seismic-9057-9348. At the well locations (CZMW8, 11; DC1), the thickness of the red and brown lines reflects the uncertainties of the weathering fronts from Gu, Mavko, et al. (2020). Profile locations are shown in Figure 1, and the three offset vertical lines show the second (600 < Vp < 2,700 m/s), third (2,700 < Vp < 4,000 m/s) and fourth (Vp > 4,000 m/s) velocity layers referred to in the text. The first layer (Vp < 600 m/s) extends from the top of layer 2 to the surface.

for the study in the Maryland Piedmont (~120–660 km). The World Stress Map shows a range for the most and least horizontal stresses at the surface (hereafter, $\sigma^f_{H,0}$ and $\sigma^f_{h,0}$) that were inferred assuming a Poisson's ratio of 1/3. The magnitudes of $\sigma^f_{H,0}$ and $\sigma^f_{h,0}$ show large local variations in some locations (Figure S4). To calculate patterns of failure potential (FP) across the entire potential range of ambient stress conditions, and to create similar models with similar stress conditions to those in St. Clair et al. (2015), we used three compression scenarios: strong ($\sigma^f_{H,0}$ = 10.8 MPa; $\sigma^f_{h,0}$ = 5 MPa), intermediate ($\sigma^f_{H,0}$ = 5.4 MPa; $\sigma^f_{h,0}$ = 2.5 MPa), and weak ($\sigma^f_{H,0}$ = 2.7 MPa; $\sigma^f_{h,0}$ = 1.25 MPa; Figure S5; Table S3). Based on the 3D stress fields, we quantified the subsurface patterns of the least compressive stress (LCS) and FP. These represent the propensities for generating or reactivating opening-mode and shear fractures, respectively (see Supporting Information).

5. Results and Discussion

Comparisons of the velocity models (Figures 2, S6 and S7) and recovered models for checkers placed at the surface (Figure 3) illustrate that Vp variations near the surface with wavelengths ≥ 5 m can be resolved along both profiles. For checkers placed at 10 mbls, the 30 and 20 m square checkers are fairly well resolved, at least under the ridges. The 10 m square checkers can also be resolved in some places along the profiles. These tests show that the depth resolution is consistent with the depth extent of dense raypath coverage, delineated as the region above the white line in Figures 3, S6 and S7. The checkers are less resolved under the valley than the ridges, consistent with the limitations in extents of ray coverage (Figures S6 and S7).

Our new logs for borehole CZMW11 and seismic models largely corroborate inferences based on full-waveform sonic logs reported for boreholes CZMW8 and 10 (Figures 1 and S2) and previously published seismic refraction profiles (Gu, Mavko, et al., 2020; West et al., 2019). A comparison of seismic models with logs for all three boreholes shows similar patterns in Vp values with respect to depth below land surface, except at ~21 and 25 mbls for well CZMW8. Those zones correlate with large fracture sets described by Gu, Mavko, et al. (2020) and Gu, Heaney, et al. (2020) (Figure S3).

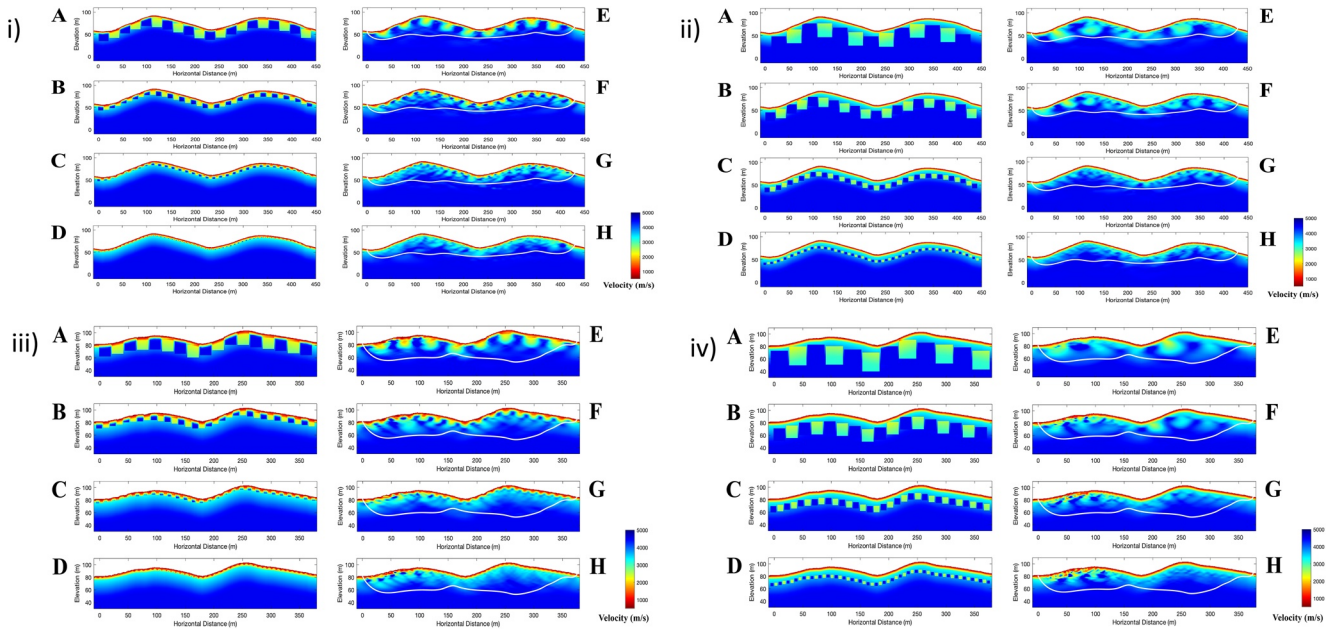

Figure 3. Checkerboard resolution tests. For each panel, (a–d) show input model, and E-H show the recovered models. The white line in the recovered models shows the depth extent of dense ray coverage taken from Figures S6 and S7. (i) Profile SH-seismic-9292-9608 with 20 (a), 10 (b), 5 (c) and 2 (d) m square checkers at the surface. (ii) Profile SH-seismic-9292-9608 with 30 (a), 20 (b), 10 (c) and 5 (d) m square checkers at 10 m depth. (iii) Profile SH-seismic-9057-9348 with 20 (a), 10 (b), 5 (c) and 2 (d) m square checkers at the surface. (iv) Profile SH-seismic-9057-9348 with 30 (a), 20 (b), 10 (c) and 5 (d) m square checkers at 10 m depth.

From all available data, models and interpretations, we note four layers: (a) the shallowest layer (decimeters to 2 m thick) with Vp < 600 m/s, (b) a middle layer with 600 < Vp < 2,700 m/s, (c) a deeper middle layer with 2,700 < Vp < ~4,000 m/s, and (4) a layer with the Vp > 4,000 m/s (Figure 2). We attribute the first layer to mobile soil, and the second and third layers to colluvium + rubbly shale that grades into fractured, chemically altered bedrock (saprock). The deepest layer (4) is attributed to bedrock where unweathered material is characterized by Vp > 4,000 m/s (Gu, Mavko, et al., 2020).

The importance of the 2,700 m/s contour was inferred previously because it was noticed that it correlates with the onset of chlorite dissolution (Gu, Mavko, et al., 2020). This observation was based on examination of a 2D seismic transect extending from ridge borehole CZMW8 to valley borehole CZMW10. Gu, Mavko, et al. (2020) argued that the 2,700 m/s contour (~6 mbls at the valley borehole and ~12–15 mbls at the ridge borehole) did not correlate with the fracture densities imaged by televiewer. Instead, Gu, Mavko, et al. (2020) pointed out it corresponds with the depth where the most reactive clay in the shale, chlorite, begins to dissolve and develop matrix porosity. We tested that observation again with our larger data set and found it applicable here: in the three boreholes intersected by our seismic profiles the depth to onset of chlorite dissolution equals 2,500 (+/− 210) m/s (Figure 2).

6. Implications for Bowtie Structure

To first order, the contours for Vp ≈ 2,000, 3,000, and 4,000 m/s in our new models mimic, rather than mirror, the topography (Figures 2, S1, S6 and S7). The profile highest in the watershed, SH-seismic-9292-9608 (Figures 2a and S6), shows that the low-velocity contours (~300 < Vp < 2,000 m/s) extend to depths ~5–10 mbls everywhere along the profile. Below that, a layer with velocities between ~2,000 and 3,000 m/s extends to deeper depths (~30 mbls) under the ridge crests than the valley (~10–15 mbls). However, the elevation of the 3,000 m/s contour is similar under ridge crests and valleys and thus does not mirror topography (Figure S1). This observation markedly contrasts that of the models from St. Clair et al. (2015) showing contours for intermediate (2,000–3,000 m/s) and higher (>3,000 m/s) velocities mirroring topography under hill-valley-hill landscapes on crystalline rock (Figure S1). The lack of support in the data for a bowtie

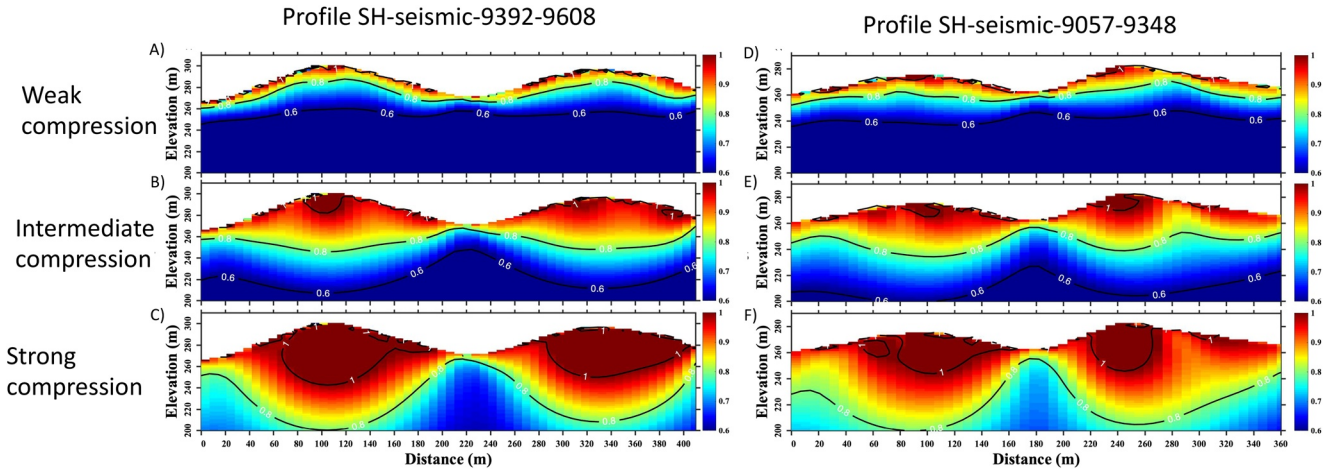

Figure 4. Failure potential for (a–c) SH-seismic-9392-9608 and (d–f) SH-seismic-9057-9348 from the 3D topographic stress model. The model scenarios are based on ambient conditions of (a), (d) weak, (b), (e) intermediate, and (c), (f) strong compression. The contours of FP = 0.6, 0.8, and 1 are shown in black lines.

structure is further illustrated in Figure S8, which shows inconsistencies between the patterns of travel times predicted for a bowtie structure and the observed travel time patterns.

Closer to the outlet, profile SH-seismic-9057-9348 (Figures 2b and S7) also shows a region with the lowest velocities (~300 < Vp < 2,000 m/s) averaging ~5–10 m in thickness. Below that, the layer with velocities between ~2,000 and 3,000 m/s extends to depths (~20 mbls) that also don't mirror the land surface (Figure S1). In addition, this layer is asymmetric, and only extends to ~5–10 mbls under the south-facing side of the southern ridge.

Although neither of the 2,000 or 3,000 m/s or higher velocity contours in the seismic profiles mirror the land surface like at Calhoun and Pond Branch (Figure S1), the modeled subsurface patterns of FP and LCS calculated for strong and intermediate stress scenarios at the same locations as the seismic lines (Figures 4 and S9) show strong bowtie patterns. For example, the contours of LCS = 0.5 MPa and FP = 0.6 to 0.8 show a bowtie similar to previous studies (Moon et al., 2017; St Clair et al., 2015), that is, the depths of relatively high failure potential are significantly deeper under ridges than under the valley (considered with respect to an arbitrary datum). The models of FP for intermediate and strong compression for Shale Hills are therefore consistent with previously calculated bowtie patterns for the Pond Brand and Calhoun sites where strong compression was also inferred (Figures 4 and S9). St. Clair et al. (2015) argued that the similarity between the predicted bowtie pattern in FP and LCS for strong and intermediate compression regimes and that of the seismic velocity pattern was strong evidence that fracture opening ± weathering explained the patterns of Vp at Pond Branch and Calhoun.

In contrast to the stronger compressional regimes, the contours of LCS = 0.5 MPa and FP = 0.6 calculated under weak compression for Shale Hills generally plot at similar absolute depths beneath ridge and valley, rising only slightly toward the surface under the valley. Likewise, the contour of FP = 0.8 for the weak compression scenario generally exhibits a subdued topographic pattern, bending slightly deeper under the ridge. These contours are more similar to our seismic results at Shale Hills (and differ markedly from those at Pond Branch and Calhoun). Thus, the correlation of the FP or LCS values with the seismic velocity profiles is strongest for the weak regime at Shale Hills (R^2 = 0.67 and 0.69, respectively, Figure S10), whereas for Pond Branch and Calhoun, the strongest correlation was found for the strong stress regime.

This result is surprising because our compilation of *in-situ* stress magnitudes show that far-field tectonic stresses are generally strongly compressive (~10 MPa) in eastern North America, and we had expected to find a bowtie structure and correlation between the FP and LCS and seismic models for the strong stress case. If the depths of Vp contours at Shale Hills are explained by stress-induced fracturing from strong compression as inferred for Pond Branch and Calhoun, then we must invoke differences among sites to explain

these observations. Possible differences in precipitation, stress regime, or rock type among the locations are discussed below.

First, climate differences such as rainfall and its effect on the water table could explain the results. For example, if the MAP were increased at Shale Hills to as high as at Pond Branch or Calhoun, the water table in Shale Hills would rise above its current level in the valley (where it varies from above the land surface in the wet season to 1–2 mbls in dry season) and under the ridges (~18–25 mbls; Sullivan et al., 2016). However, this higher water table would make the Vp contours even less like mirrors of the land surface. If the water table rose, the intermediate layer of saprock (with ~6%–8% porosity; Gu, Mavko, et al., 2020) would partially or completely saturate with water, increasing the P-wave velocities by as much as 500 m/s above today's values. In this case, given the differences in the depth to the water table between the valley floor (1–2 mbls) and ridge crests (18–25 mbls), velocity contours in areas above the water table under the ridge crests would be at depths ~5–10 m shallower (i.e., nearer the land surface) than shown in Figure 2. The velocity contours for higher MAP would thus mimic the topography even more closely, as opposed to mirror it.

Another possible explanation is that stress conditions in Shale Hills from the Appalachian ridge and valley province could be lower than those of the Piedmont watersheds if local, rather than regional, effects dominated. Inferred horizontal stress magnitudes at the surface from the World Stress Map (Haimson, 1977; Heidbach et al., 2016) generally decrease from the northeastern United States to Canada, and thus could be higher in the two southern Piedmont locations. In addition, elevated seismic activity in the Central Virginia and Charleston seismic zones may imply potentially higher stress magnitudes in the Piedmont (Mazzotti & Townend, 2010). Likewise, *in-situ* stress magnitudes could be influenced in complex ways by plate tectonics, past glacial loading and unloading, and local variations in structure (Ghosh et al., 2019; Miller & Dunne, 1996; Stewart et al., 2000; Zoback, 1992). For example, although none of the watersheds (Shale Hills, Pond Branch, Calhoun) were glaciated, central Pennsylvania was close to the margin of the Laurentide ice sheet where horizontal stresses could have been reduced because of glacial isostatic adjustment (Muir-Wood, 2000; Stewart et al., 2000; Wu & Hasegawa, 1996). Yet another stress-related explanation is that systematic, regional joint sets in the Valley and Ridge Province (Nickelsen & Hough, 1967) may have induced locally weak compressional stresses in certain areas (Engelder, 1982; Pollard & Segall, 1987).

Alternatively, the shale in Shale Hills might deform more readily than the crystalline rock in either Pond Branch or Calhoun, reducing the stresses locally. For example, Pond Branch, the watershed closest to Shale Hills geographically and climatically, is developed on schist, a rock type known to have a higher modulus ratio than shale (Goodman, 1989). If this explanation is correct, then the regional compressional regime might be strong, as originally expected, but the shale may have accommodated the strong compression locally by generating macroscopic fractures or microcracks.

However, we observed very few microcracks in thin sections of saprock from the site (Gu, Rempe, et al., 2020). We did see evidence for enhanced weathering around isolated large fractures in the shale at depth, and we have argued this latter observation is consistent with rate limitation of weathering of the saprock by fracture formation (Gu, Heaney, et al., 2020). But given that the macrofractures in televiewer images do not correlate with Vp patterns (Gu, Mavko, et al., 2020), the density of macrofractures alone does not provide sufficient explanation for the lower Vp values in the surficial layers of the watershed.

In contrast to fractures, both weathering and subsurface degassing of bubbles correlate with slow Vp in the shale. Specifically, Gu, Mavko, et al. (2020) attributed Vp $<$ 600 m/s to disaggregation of saprock, Vp $<$ 2,700 m/s to dissolution of chlorite, and changes in Vp in the deeper saprock from 2,700 to 4,500 m/s to a combination of gas bubbles $\pm$ pores $\pm$ fractures. In many parts of the landscape and at many depths, the slowing of Vp in the near-surface correlates with observable weathering reactions more than observable fracturing.

7. Summary and Conclusions

Variations in P-wave velocities along two seismic refraction profiles crossing the well-studied Shale Hills watershed located in the Valley and Ridge province were compared with predictions of failure potential from a stress model to evaluate the importance of coupled tectonic-topographic fracturing. To explain the

lack of a bowtie structure in the subsurface inferred from these data, significantly weaker stress conditions in central Pennsylvania are required when compared to predicted regional stress magnitudes. If the topographic stress-induced fracture model is applicable to Shale Hills, it implies a weak compressional regime, which could arise from a local deviation in the regional stress field or from the enhanced deformability of shale, as opposed to crystalline bedrock. The lack of a bowtie-like subsurface velocity pattern at Shale Hills could document that other factors such as infiltration of deeply flowing oxygenated waters are more important than topographic-induced fracturing in explaining depths of weathering in sedimentary rock.

Data Availability Statement

Seismic data are available from the IRIS Data Management Center and borehole logs from the Shale Hills CZO webpage (http://www.czo.psu.edu/data_geochemical_geophysical.html). IRIS Passcal Instrument Center provided seismic equipment and logistical and data support.

Acknowledgments
Funding is acknowledged from DOE OBES DE-FG02-05ER15675 and NSF EAR grants 12-39285, 13-31726 to S. L. Brantley and 19-45431, 20-12073 to S. Moon Shale Hills, part of Penn State's Stone Valley Forest, is facilitated by the College of Agricultural Sciences and Department of Ecosystem Science and Management. C. Cole, J. Grant, K. Lutz, and J. Renzaglia helped with P-wave-arrival picking. We thank Mon-Han Huang and Roy Johnson for helpful reviews.

References

Brantley, S. L., White, T. S., West, N., Williams, J., Forsythe, B., Shapich, D., et al. (2018). Susquehanna Shale Hills Critical Zone Observatory: Shale Hills in the Context of Shaver's Creek Watershed. *Vadose Zone Journal*, *17*, 180092. https://doi.org/10.2136/vzj2018.04.0092

Engelder, T. (1982). Is there a genetic relationship between selected regional joints and contemporary stress within the lithosphere of North America? *Tectonics*, *1*, 161–177. https://doi.org/10.1029/tc001i002p00161

Ghosh, A., Holt, W. E., & Bahadori, A. (2019). Role of large-scale tectonic forces in intraplate earthquakes of central and eastern North America. *Geochemistry, Geophysics, Geosystems*, *20*, 2134–2156. https://doi.org/10.1029/2018gc008060

Goodman, R. E. (1989). *Introduction to rock mechanics* (p. 562). JohnWiley.

Gu, X., Heaney, P. J., Reis, F. D. A., & Brantley, S. L. (2020). Deep abiotic weathering of pyrite. *Science*, *370*(6515). https://doi.org/10.1126/science.abb8092

Gu, X., Mavko, G., Ma, L., Oakley, D., Accardo, N., Carr, B. J., et al. (2020). Seismic refraction tracks porosity generation and possible CO_2 production at depth under a headwater catchment. In: *Proceedings of the National Academy of Sciences of the United States of America*. Retrieved from https://www.pnas.org/content/early/2020/07/23/2003451117

Gu, X., Rempe, D. M., Dietrich, W. E., West, A. J., Lin, T.-C., Jin, L., & Brantley, S. L. (2020). Chemical reactions, porosity, and microfracturing in shale during weathering: The effect of erosion rate. *Geochimica et Cosmochimia Acta*, *269*, 63–100. https://doi.org/10.1016/j.gca.2019.09.044

Haimson, B. C. (1977). Crustal stress in the continental United States as derived from hydrofracturing tests. In J. G. Heacock, G. V. Keller, J. E. Oliver, & G. Simmon (Eds.), *The Earth's crust* (pp. 576–592). American Geophysical Union. https://doi.org/10.1029/GM020p0576

Heidbach, O., Rajabi, M., Reiter, K., Ziegler, M., & Team, W. (2016). World Stress Map Database Release 2016 (Vol. 10). GFZ Data Services.

Herndon, E. M., Steinhoefel, G., Dere, A. L. D., & Sullivan, P. L. (2018). Perennial flow through convergent hillslopes explains chemodynamic solute behavior in a shale headwater catchment. *Chemical Geology*, *493*, 413–425. https://doi.org/10.1016/j.chemgeo.2018.06.019

Holbrook, S. W., Riebe, C. S., Elwaseif, M., Hayes, J. L., Basler-Reeder, K., Harry, D. L., et al. (2013). Geophysical constraints on deep weathering and water storage potential in the Southern Sierra critical zone observatory. *Earth Surface Processes and Landforms*, *39*, 366–380. https://doi.org/10.1002/esp.3502

Ma, L. (2020). *P-wave velocity structure of the Shale Hills Watershed (M.S. Thesis)* (p. 226). The Pennsylvania State University.

Mazzotti, S., & Townend, J. (2010). State of stress in central and eastern North American seismic zones. *Lithosphere*, *2*, 76–83. https://doi.org/10.1130/L65.1

Miller, D. J., & Dunne, T. (1996). Topographic perturbations of regional stresses and consequent bedrock fracturing. *Journal of Geophysical Research*, *101*(25), 523–536. https://doi.org/10.1029/96JB02531

Moon, S., Perron, J. T., Martel, S. J., Goodfellow, B. W., Mas Ivars, D., Hall, A., et al. (2020). Present-day stress field influences bedrock fracture openness deep into the subsurface. *Geophysical Research Letters*, *47*. https://doi.org/10.1029/2020GL090581

Moon, S., Perron, T., Martel, S. J., Holbrook, W. S., & St Clair, J. (2017). A model of three-dimensional topographic stresses with implications for bedrock fractures, surface processes, and landscape evolution. *Journal of Geophysical Research: Earth Surface*, *122*, 823–846. https://doi.org/10.1002/2016JF004155

Muir-Wood, R. (2000). Deglaciation seismotectonics: A principal influence on intraplate seismogenesis at high latitudes. *Quaternary Science Reviews*, *19*, 1399–1411. https://doi.org/10.1016/s0277-3791(00)00069-x

Nickelsen, R. P., & Hough, V. N. D. (1967). Jointing in the Appalachian plateau of Pennsylvania. *The Geological Society of America Bulletin*, *78*, 609–630. https://doi.org/10.1130/0016-7606(1967)78[609:jitapo]2.0.co;2

Nolet, G. (1987). Seismic wave propagation and seismic tomography. In G. Nolet, & Reidel (Eds.), *Seismic tomography* (pp. 1–23). Springer. https://doi.org/10.1007/978-94-009-3899-1_1

Oakley, D., Forsythe, B., Gu, X., Nyblade, A., & Brantley, S. L. (2021). Seismic ambient noise analyses reveal changing temperature and water signals to 10s of meters depth in the critical zone. *Journal of Geophysical Research: Earth Surface*, *126*. https://doi.org/10.1029/2020JF005823

Parsekian, A. D., Singha, K., Minsley, B. J., Holbrook, W. S., & Slater, L. (2015). Multiscale geophysical imaging of the critical zone. *Reviews of Geophysics*, *53*, 1–26. https://doi.org/10.1002/2014RG000465

Pollard, D. D., & Segall, P. (1987). Theoretical displacements and stresses near fractures in rock: With applications to faults, joints, veins, dikes, and solution surfaces. In: *Fracture mechanics of rock* (pp. 277–349). https://doi.org/10.1016/b978-0-12-066266-1.50013-2

Reibe, C. S., Hahm, W. J., & Brantley, S. L. (2017). Controls on deep critical zone architecture: A historical review and four testable hypotheses. *Earth Surface Processes and Landforms*, *42*, 128–156. https://doi.org/10.1002/esp.v42.8

Slim, M., Perron, J. T., Martel, S. J., & Singha, K. (2015). Topographic stress and rock fracture: A two dimensional numerical model for arbitrary topography and preliminary comparison with borehole observations. *Earth Surface Processes and Landforms*, *40*, 512–529. https://doi.org/10.1002/esp.3646

St Clair, J., Moon, S., Holbrook, S. W., Perron, J. T., Riebe, C. S., Martel, S., et al. (2015). Geophysical imaging reveals topographic stress control of bedrock weathering. *Science*, *350*, 534–538. https://doi.org/10.1126/science.aab2210

Stewart, I. S., Sauber, J., & Rose, J. (2000). Glacio-seismotectonics: Ice sheets, crustal deformation and seismicity. *Quaternary Science Reviews*, *19*, 1367–1389. https://doi.org/10.1016/s0277-3791(00)00094-9

Sullivan, P. L., Hynek, S., Gu, X., Singha, K., White, T. S., West, N., et al. (2016). Oxidative dissolution under the channel leads geomorphological evolution at the Shale Hills catchment. *American Journal of Science*, *December*, 981–1026. https://doi.org/10.2475/10.2016.02

Thomas, A. L. (1993). *Poly3D: A three-dimensional, polygonal element, displacement discontinuity boundary element computer program with applications to fractures, faults, and cavities in the Earth's crust*. Stanford University.

Vidale, J. E. (1990). Finite-difference calculation of traeltimes in three dimensions. *Geophysics*, *55*, 521–526. https://doi.org/10.1190/1.1442863

West, N., Kirby, E., Bierman, P., Slingerland, R., Ma, L., Rood, D., & Brantley, S. L. (2013). Regolith production and transport at the Susquehanna Shale Hills critical zone observatory: Part 2 - Insights from meteoric ^{10}Be. *Journal of Geophysical Research, Earth Surface*, *118*, 1877–1896. https://doi.org/10.1002/jgrf.20121

West, N., Kirby, E., Nyblade, A., & Brantley, S. L. (2019). Climate preconditions the Critical Zone: Elucidating the role of subsurface fractures in the evolution of asymmetric topography. *Earth and Planetary Science Letters*, *513*, 197–205. https://doi.org/10.1016/j.epsl.2019.01.039

Wu, P., & Hasegawa, H. S. (1996). Induced stresses and fault potential in eastern Canada due to a disc load: A preliminary analysis. *Geophysical Journal International*, *125*, 415–430. https://doi.org/10.1111/j.1365-246X.1996.tb00008.x

Zelt, C. A., Azaria, A., & Levander, A. (2006). 3D seismic refraction traveltime tomography at a groundwater contamination site. *Geophysics*, *71*, H67–H78. https://doi.org/10.1190/1.2258094

Zelt, C. A., & Barton, P. J. (1998). Three-dimensional seismic refraction tomography: A comparison of two methods applied to data from the Faeroe Basin. *Journal of Geophysical Research*, *103*, 7187–7210. https://doi.org/10.1029/97jb03536

Zoback, M. L. (1992). Stress field constraints on intraplate seismicity in eastern North America. *Journal of Geophysical Research*, *97*, 11761–11782. https://doi.org/10.1029/92jb00221